Core-shell nanospheres under visible light: Optimal absorption, scattering, and cloaking

Arsen Sheverdin and Constantinos Valagiannopoulos*
Department of Physics, School of Science and Technology, Nazarbayev University, 53 Qabanbay Batyr Avenue, Astana KZ-010000, Kazakhstan

(Received 4 December 2018; revised manuscript received 14 January 2019; published 19 February 2019)

Discovering peak-performing components, under certain structural and material constraints, is vital for the efficient operation of integrated systems that incorporate them. This becomes feasible by comprehensive scanning of the parametric space for one of the simplest classes of three-dimensional particles used in visible-light metasurface applications: the core-shell nanosphere. For each combination of actual media picked from a long list, the highest-scoring nanoparticles in terms of absorbance, scattering, and cloaking are recorded, while their near-field visualizations unveil the resonance mechanisms that make them so special. The reported results offer additional degrees of freedom in modeling collective meta-atom interactions and contribute to the photonic inverse design by providing the upper limits in the performance for particles of a basic geometry.

DOI: 10.1103/PhysRevB.99.075305

I. INTRODUCTION

Placing many identical (or not) small particles across a surface makes an illusion of extraordinary boundary conditions, which is the principle of metasurfaces with their countless utilities [1]. Collective operation of these inclusions placed in lattice configurations can dramatically change the electric and magnetic field components from both sides of the lattice, leading to reformulating reflection and refraction laws, admitting arbitrary field transformations [2]. That ability to tailor and manipulate local fields in a subwavelength domain also makes these tiny objects exceptional building blocks of integrated optical circuits that process information at the nanometer scale [3]. Suitably selected and carefully distributed particles can finally build powerful metamaterial platforms achieving complete control of wave amplitude, phase with subwavelength spatial resolution, the key feature behind multiple nanophotonic elements [4].

Among numerous candidate particles, core-shell spheres are placed prominently for reasons related to analytical solvability permitting efficient optimizations and symmetry dictating angle insensitivity. Such a structure, possessing two volumes (internal and external), provides the minimal condition to support resonance effects being responsible for any extremum in the device's performance. According to rigorous Mie theory, the response of a small core-shell nanosphere comprises two terms corresponding to electric and magnetic dipoles; once each of them gets maximized, the respective (electric or magnetic) Mie resonance occurs [5,6]. When both of the terms are small, the particle gives a minimum overall response which, if appears in the wavelength vicinity of either of the two maxima, yields to asymmetric line shape, an identity characteristic of the so-called Fano resonance [7]. Finally, if the permittivities of the core and the shell are of opposite sign, the well-known surface plasmon resonance [8] can manifest itself through large signal concentration on the plasmonic/dielectric boundary.

Such resonance effects always accompany particle's extreme responses in terms of its two basic operations: scattering and absorption. The scattering from a core-shell nanosphere determines the way it is perceived by its external world; thus, it has attracted substantial attention [9] and helped in the formulation of more general treatments concerning larger classes of meta-atoms [10]. In particular, superscattering by spherical nanoparticles has been reported by superimposing multiple resonances corresponding to different total angular momenta [11,12] and utilizing nonlocal coatings [13]. Absorption, on the other hand, is associated to what is happening inside the lossy particle and is crucial when conversion of electromagnetic energy to thermal or other forms is required. As a result, boosting light trapping by core-shell nanospheres has been extensively examined in various contexts, involving plasmon-exciton interactions [14] or total internal reflection in thin films [15]. Importantly, high losses do not necessarily imply substantial absorptivity since the field gets "discouraged" from entering the conducting volume owing to the large impedance mismatch with the lossless background. That matching condition is also a prerequisite for cloaking in core-shell particles which dictates minimum scattering power and very low losses, a rather challenging combination. The well-established scattering cancellation technique [16] makes a spherical volume transparent via coating it with a layer of suitable thickness and texture but only at a specific frequency; indeed, the cumulative scattering by an object across the entire electromagnetic spectrum is an increasing function of its size [17].

The core-shell resonant nanospheres with considerable absorbing, scattering, or cloaking scores can be used in a number of different applications. As far as absorption is concerned, similar particles are employed in photovoltaics; broadband light collection occurs in the host thin-film solar cells [18] assisted by developed surface plasmons and followed by energy conversion into energetic electrons and holes at

*konstantinos.valagiannopoulos@nu.edu.kz

the nearby semiconductor [19]. Furthermore, photothermal therapy, namely, the selective killing of cancer cells through heat concentration, has been accomplished [20] with highly absorbing core-shell nanospheres, which can be additionally used to improve the efficacy of other light-activated biological treatments [21]. When it comes to spherical particles scattering response, it is the basis of several nanodevice models for data-storage units facilitated by photon tunable energy-level upconversion [22] or multicolor labeling and tagging in optical imaging [23]. When the core-shell spherical geometry is properly combined with nonlinear materials, one can also achieve huge scattering switching [24] or enhanced second-order harmonic generation [25], while filling the core with a gain medium makes emitters with fast spontaneous emission feeding plasmonic nanoantennas [26].

In this work, we regard such a simple but multifunctional structure as the core-shell nanosphere, illuminated by visible light and made of actual media with realistic losses. We consider a set of available materials and, for each core-shell combination of them, we pick the most efficient designs in terms of absorption and (high or low) scattering by recording their physical sizes and the operational wavelength. As our optimization routine scans the visible spectrum, the permissible range of the particle's radius changes accordingly to capture nanospheres with optical size neither too small, yielding a non-negligible response, nor too big to support coherent operation in metasurface lattices. We report numerous nanospheres working at various colors of incoming light that absorb or scatter tenfold the incoming power passing through their geometrical cross section, while our cloaked meta-atoms perturb the background field by less than 1%. The variety of the presented alternative designs combined with their high fabrication potential through physical [27] and chemical [28] methods provides additional degrees of freedom in modeling and realization of multiobjective metasurfaces.

This study tests the limits of a significant class of particles by exhaustively searching across a quite extended parametric space including a long list of materials and the entire spectrum of visible frequencies. Importantly, the optical size of the considered inclusions is free to vary within a substantial value range meeting the requirements of practically all metasurface applications. The proposed optimal designs do not necessarily correspond to universal maxima in absorbing and scattering performance of core-shell nanospheres [29]; however, they certainly hit high scores which can only be surpassed by more complex designs in structure or texture [30]. Therefore, we believe that our work contributes to the recent paradigm shift of photonic inverse design [31,32] by focusing on simple shapes and actual media.

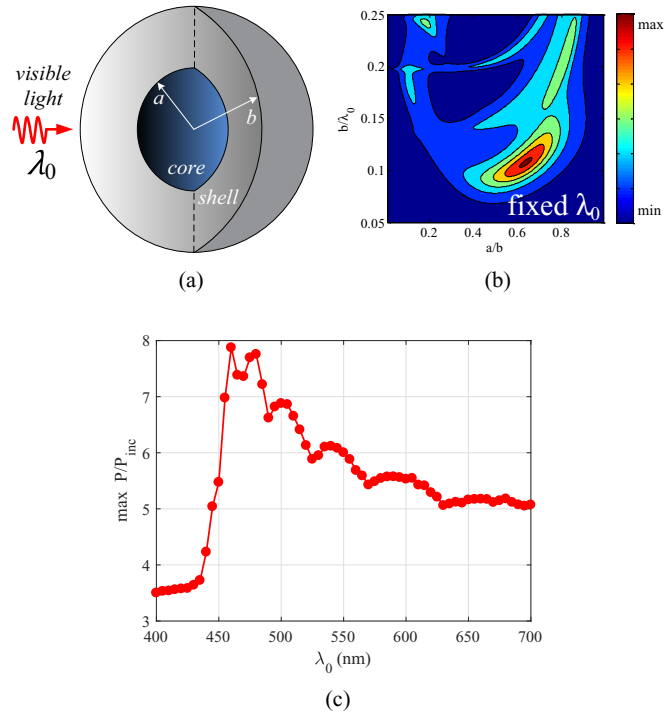

FIG. 1. (a) The structural model of a core-shell nanosphere illuminated by a plane wave of visible light. (b) Typical variation of absorbed/scattering power metric P/P_{inc} with respect to aspect ratio a/b and optical size b/λ_0 for fixed materials and wavelength. (c) Typical variation of maximum P/P_{inc} as a function of operational wavelength λ_0 for fixed materials.

II. FORMULATION AND METHOD

A. Fields and power

Consider a spherical particle comprised of a core with radius a covered by cladding of thickness $(b-a)$, illuminated by visible light in the form of a monochromatic plane wave (with oscillating frequency ω) traveling into free space [as in Fig. 1(a)]. The dispersive relative complex permittivities of the core $(r<a)$ and the shell $(a<r<b)$ are denoted by $\varepsilon_1=\varepsilon_1(\omega)$ and $\varepsilon_2=\varepsilon_2(\omega)$, respectively. The symbols (r,θ,φ) are used for the related spherical coordinates, while the equivalent Cartesian ones read (x,y,z); the suppressed harmonic time is of the form $e^{+i\omega t}$. For simplicity and without loss of generality (due to the spherical symmetry), we assume that the incident wave propagates along the $+z$ axis and its electric field vector is always parallel to the x axis oscillating with amplitude $E_0>0$ (measured in volts per meter). This background field can be decoupled into two field terms, each of which satisfies Maxwell's laws: one term with no radial electric component (TE) and another one with no radial magnetic component (TM). These terms can be expressed as series of spherical harmonics, which dictate the $\theta-$ and $\varphi-$ dependence of the field quantities in all the regions defined by the concentric and entire surfaces (rigorous Mie theory). After imposing the necessary boundary conditions, the scattered fields for $r>b$ (electric field vector of the TE set and magnetic one for the TM set) take the forms

$$\mathbf{E}^{\text{TE}}_{\text{scat}}=E_0\sum_{n=1}^{+\infty}S_n^{\text{TE}}h_n(k_0r)\begin{Bmatrix}-\hat{\boldsymbol{\theta}}\csc\theta P_n(\theta)\cos\varphi\\ +\hat{\boldsymbol{\varphi}}P_n'(\theta)\sin\varphi\end{Bmatrix},$$

$$\mathbf{H}^{\text{TM}}_{\text{scat}}=\frac{E_0}{\eta_0}\sum_{n=1}^{+\infty}S_n^{\text{TM}}h_n(k_0r)\begin{Bmatrix}-\hat{\boldsymbol{\theta}}\csc\theta P_n(\theta)\sin\varphi\\ -\hat{\boldsymbol{\varphi}}P_n'(\theta)\cos\varphi\end{Bmatrix},$$

where $P_n(\theta)$ is the Legendre polynomial of first order, degree n, and argument $\cos\theta$, and h_n is the spherical Hankel function of order n and second type. The symbols $k_0=2\pi/\lambda_0$ and η_0 stand for the wave number and the wave impedance into

vacuum. The coefficients $S_n^{\mathrm{TE/TM}}$, are complex dimensionless quantities and not shown here for brevity [16].

The power P_{scat} carried by the TE and TM scattered component into vacuum (which constitutes a self-consistent electromagnetic field), expresses how much the sphere perturbs the background field distribution externally to it. It can be easily computed with the use of Poynting's theorem and expansions of $h_n(k_0 r)$ for large arguments $k_0 r \gg 1$ (in the far region), as follows (Ref. [33], pp. 102–104):

$$P_{\mathrm{scat}} = W \sum_{n=1}^{+\infty} \frac{n^2(n+1)^2}{2n+1} \left(\left| S_n^{\mathrm{TE}} \right|^2 + \left| S_n^{\mathrm{TM}} \right|^2 \right), \tag{1}$$

where $W = \frac{\pi E_0^2}{k_0^2 \eta_0} > 0$ is a quantity measured in watts. The power absorbed by the particle, given the fact that one or both of the constituent media is lossy, namely, $\mathrm{Im}[\varepsilon_1] \neq 0$ or $\mathrm{Im}[\varepsilon_2] \neq 0$, is evaluated by applying again Poynting's theorem, but for the total field into free space this time. Indeed, if we integrate the power spatial density across any sphere of radius $r > b$ (even the infinite $k_0 r \to +\infty$ one), we obtain

$$P_{\mathrm{abs}} = -P_{\mathrm{scat}} - W \sum_{n=1}^{+\infty} n(n+1) \mathrm{Re}\left[i^n \left(S_n^{\mathrm{TE}} + S_n^{\mathrm{TM}} \right) \right]. \tag{2}$$

Obviously, $P_{\mathrm{scat}}, P_{\mathrm{abs}} > 0$, which means that the series in Eq. (2) should converge to negative values smaller than $(-P_{\mathrm{scat}}/W)$. In the absence of any losses, we have $P_{\mathrm{abs}} = 0$ and the aforementioned sum is equal to $(-P_{\mathrm{scat}}/W)$.

In order to render the absorbed and scattered power more meaningful, we should normalize them by suitable quantities. More specifically, we can use as a reference parameter the power of the incident illumination passing through the geometrical cross of the scatterer, namely, $P_{\mathrm{inc}} = \frac{\pi E_0^2 b^2}{2\eta_0}$. The ratio $P_{\mathrm{abs}}/P_{\mathrm{inc}}$ is equal to the absorption cross section (Ref. [33], pp. 69–77) of the particle σ_{abs} over the area of the sphere as seen by the incoming plane wave (πb^2). Similarly, P_{scat} is normalized by the same quantity and we obtain the metric $P_{\mathrm{scat}}/P_{\mathrm{inc}}$ which equals the scattering cross section σ_{scat} (measured in square meters) again normalized by (πb^2).

B. Maximization scheme

Our aim is to consider numerous bulk media which are available for applications in the visible part of the wavelength spectrum, $400 < \lambda_0 < 700$ nm, by taking into account their frequency-dispersive behavior. The materials are selected based on their electromagnetic diversity and experimental relevance as usual [34]. From this large set of employable materials, we would like to pick those combinations, in suitably sized core-shell nanospheres, which overdeliver in terms of absorption and scattering. Our results could serve as a directory of maximal performances under the condition of using real media in simple two-layered structures and as benchmarks for smarter designs to pass.

We follow a systematic approach that scans all the regarded wavelengths λ_0 and, for each of them, selects the configuration of dimensions (a, b) giving maximal $P_{\mathrm{abs}}/P_{\mathrm{inc}}$ or $P_{\mathrm{scat}}/P_{\mathrm{inc}}$. In the optimization, we do not avoid homogeneous spheres solely made of one material $(a/b \to 0, 1)$ and thus $0 < a/b < 1$; for the size of the nanosphere, on the contrary, we pose an upper bound of half wavelength and exclude too-small structures $(0.05 < b/\lambda_0 < 0.25)$. A typical variation of our metrics P/P_{inc} on an $(a/b, b/\lambda_0)$ map is depicted in Fig. 1(b) at fixed λ_0. From several local maxima, we select the strongest one and we store it (together with the dimensions of the regarded design) as the best performance that can be achieved by a specific pair of materials for the considered operational wavelength λ_0. The aforementioned global maximum corresponds to one point in the graph of Fig. 1(c), where the highest scores P/P_{inc} for each wavelength are shown as a function of λ_0. Potential abrupt changes of the curve are attributed to the fact that the represented quantity $\max_{\{0<a/b<1\,,\,0.05\lambda_0<b<0.25\lambda_0\}} P/P_{\mathrm{inc}}$ is an outcome of maximization and thus no smooth behavior is necessarily expected. From the graph of Fig. 1(c), we pick only one ultraperforming design for absorption or scattering with certain frequency preference.

It should be stressed that, unlike the inequality $0 < a/b < 1$ that is imposed by the structure, the constraint $0.05 < b/\lambda_0 < 0.25$ is an artificial one. In particular, extremely small sizes $b/\lambda_0 \to 0$ usually give very weak scatterers and absorbers, while nanospheres bigger than $\lambda_0/2$ cannot serve as unit cells for collective operation in metasurfaces, arrays, and networks [35]. As has been mentioned [36], no lower limit for b means that the best performance emerges for a resonant atom with its extremely tiny size. Therefore, on certain occasions, the largest value of P/P_{inc} across the rectangular plane of Fig. 1(b) is recorded for the low limit $b/\lambda_0 = 0.05$, which means that the true maximum is exhibited for a small particle outside of the considered map. If the maximum of the curve in Fig. 1(c) happens for such a case, we check secondary peaks to neighboring (or not) wavelengths. Therefore, the reported overdelivering structures always correspond to an interior (not boundary) extremum to the map of Fig. 1(b), which sometimes emerges for $b/\lambda_0 \cong 0.05$.

Our search for optimal designs contains several materials including bulk metals, semiconductors, and inorganic dielectrics, for which permittivity profiles are obtained from a well-known material database [37], containing measurements from established references [38,39]. In the following, we assume that the dielectric constants ε_1 and ε_2 of our media remain the same at a specific wavelength λ_0, regardless of the layer thicknesses. Certain corrections to the damping of metals by taking into account the shape and the size of the samples are possible [40]; however, given the relatively large diameter of the particles (at least 40 nm or 10% of the operational wavelength), we assume such an influence to be of restricted importance.

The two materials in such a simple design should be chosen as different as possible $(\mathrm{Re}[\varepsilon_1]\mathrm{Re}[\varepsilon_2] < 0)$; otherwise the conditions for resonance [3] cannot be fulfilled. Therefore, from the aforementioned available media, we have concluded that the most remarkable performances related to absorption and scattering emerge for combining a metal in the visible with a nonplasmonic material, regardless of their relative position (shell or core). This placement-indifference feature can be attributed to the way that the field "embraces" the sphere as a finite-size scatterer which, unlike the infinite nanowire case [41], supports symmetric interplay between the response from any two antipodal points of its surface. By trying every single

TABLE I. Optimally absorbing nanospheres with metallic cores (ε_1, different rows) and dielectric shells (ε_2, different columns). Performance $P_{\rm abs}/P_{\rm inc}$ at specific wavelengths λ_0 (indicated also by the corresponding color of the visible spectrum) and optimal geometric sizes (a, b) for each combination of the available materials at which the proposed core-shell sphere of Fig. 1(a) absorbs maximally the incident field. Shaded boxes denote poor performance.

ABSORPTION Core/Shell	**Aluminium antimonide (AlSb)**	**Cadmium sulfide (CdS)**	**Iron(III) oxide (Fe_2O_3)**	**Iron(II,III) oxide (Fe_3O_4)**	**Gallium arsenide (GaAs)**	**Gallium phosphide (GaP)**	**Titanium oxide (TiO_2)**
Silver (Ag)	6.50 @ 670 nm $b/\lambda_0 = 0.070$ $a/b = 0.66$	6.70 @ 530 nm $b/\lambda_0 = 0.070$ $a/b = 0.54$	4.64 @ 625 nm $b/\lambda_0 = 0.086$ $a/b = 0.62$	9.63 @ 420 nm $b/\lambda_0 = 0.052$ $a/b = 0.80$	4.48 @ 515 nm $b/\lambda_0 = 0.082$ $a/b = 0.86$	10.40 @ 530 nm $b/\lambda_0 = 0.051$ $a/b = 0.73$	10.31 @ 470 nm $b/\lambda_0 = 0.051$ $a/b = 0.66$
Gold (Au)	5.92 @ 700 nm $b/\lambda_0 = 0.074$ $a/b = 0.70$	4.21 @ 585 nm $b/\lambda_0 = 0.086$ $a/b = 0.68$				5.89 @ 685 nm $b/\lambda_0 = 0.074$ $a/b = 0.62$	4.18 @ 590 nm $b/\lambda_0 = 0.090$ $a/b = 0.66$
Copper (Cu)	5.93 @ 690 nm $b/\lambda_0 = 0.073$ $a/b = 0.72$	4.67 @ 600 nm $b/\lambda_0 = 0.082$ $a/b = 0.64$	4.90 @ 630 nm $b/\lambda_0 = 0.082$ $a/b = 0.72$			6.374 @ 64 nm $b/\lambda_0 = 0.069$ $a/b = 0.70$	4.65 @ 605 nm $b/\lambda_0 = 0.082$ $a/b = 0.60$

combination of media, we check the behavior of the device across all the operating wavelengths λ_0 and, through the optimization process described above, we conclude to a single design working at a specific wavelength. In this way, the tables presented in the following are populated and contain the best cases corresponding to each core-shell pair of materials. It should be stressed that we may miss a highly performing design for a certain wavelength because a better one appears at another wavelength; however, the obtained results cover the entire visible part of the frequency spectrum.

The aforementioned optimization approach can be employed in more general inverse design schemes with alternative metrics [instead of the scattering (1) or absorbed power (2)] related to the examined response like the epsilon-near-zero (ENZ) features of the considered particles, which accompany numerous interesting interactions [42,43]. Moreover, the presented methodology may be modified to detect not only ultraperforming isolated core-shell nanospheres but also metasurfaces made of many of them, working collectively; indeed, the collective polarizability of a meta-atom is analytically expressed in terms of the individual one [44]. Further minor adjustments can be made if the particles are not free standing but the background incorporates other passive structures, like a dielectric substrate, commonly utilized when a metasurface is actually fabricated.

C. Available fabrication techniques

Prior to introducing the results of the proposed optimization, it is worth briefly discussing the potential fabrication methods of core-shell particles, made from a number of media. Even in the visible, there are several ways of shaping multilayered nanospheres [45], given the fact that spherical geometry provides a minimum surface area for a given volume, a rather natural preference.

One large set of methods in fabricating core-shell nanoparticles concerns chemical reactions that occur across the surface of the core producing the suitable engulfing cladding. In particular, oxide shells of controllable thicknesses are developed around metallic spheres via hydrolysis of the related precursors [28], while the metal passivation method followed by deposition of surface active agents leads to construction of similar meta-atoms [46]. Furthermore, an efficient two-step process of coat synthesis on plasmonic colloids has been proposed, yielding to stable particles able to get transferred into any solvent [47]. In addition, nanospheres in dimer pairs can be also self-assembled, since different substances tend to adhere to each other, mutually react, and form hybrid structures [48]. Moreover, colloidal meta-atoms with controlled density can be grown on thin films via the Langmuir-Schaefer technique [49] or electron-beam-induced deposition [50], which do not necessarily concern nanoparticles of spherical shape [50,51].

Apart from the aforementioned techniques, one can follow physical fabrication methods by directly depositing the desired media around spherical cores without relying on chemical reactions. More specifically, core-shell nanoparticles can be prepared through a solution-based template wetting method by exploiting the different interaction degree of the two comprising media with water [27]. Finally, gas-phase synthesis makes a low-cost alternative approach according to which the core gets combusted and its molecules are sprayed with the suitable covering medium in gas form [52].

In most of the cases described above, the core is metallic, which is quite a common choice; however, note that designs of plasmonic shells are also realizable. In particular, metal colloids can be deposited around oxides with help from suitable acidic layers placed in-between [53,54] or by employing picosecond laser and ultrasonic wave generation in a deionized water bath [55].

III. OPTIMAL ABSORPTION

In Table I, we show the best designs for each combination of metallic cores (ε_1) and semiconducting or dielectric coats (ε_2) operated at specific wavelengths whose color paints the corresponding cell. Shaded boxes correspond to poor absorption performance. One directly notices that silver, due to its low losses and strong plasmonic nature [56], can adjust itself to resonate with all the available claddings and at different visible wavelength each time. In general, the moderate magnitude of losses, even for the semiconducting

TABLE II. Optimally absorbing (maximum P_{abs}/P_{inc}) nanospheres with dielectric cores (ε_1, different columns) and metallic shells (ε_2, different rows).

ABSORPTION Shell/Core	Air	Aluminium(III) oxide (Al_2O_3)	Cadmium sulfide (CdS)	Iron(III) oxide (Fe_2O_3)	Iron(II,III) oxide (Fe_3O_4)	Gallium phosphide (GaP)	Titanium oxide (TiO_2)
Silver (Ag)			8.53 @ 520 nm $b/\lambda_0 = 0.050$ $a/b = 0.67$	7.06 @ 690 nm $b/\lambda_0 = 0.053$ $a/b = 0.78$	8.88 @ 445 nm $b/\lambda_0 = 0.050$ $a/b = 0.56$	7.79 @ 535 nm $b/\lambda_0 = 0.050$ $a/b = 0.55$	8.60 @ 415 nm $b/\lambda_0 = 0.051$ $a/b = 0.41$
Gold (Au)	8.93 @ 610 nm $b/\lambda_0 = 0.050$ $a/b = 0.863$	8.40 @ 665 nm $b/\lambda_0 = 0.051$ $a/b = 0.84$	4.41 @ 590 nm $b/\lambda_0 = 0.078$ $a/b = 0.640$	5.46 @ 700 nm $b/\lambda_0 = 0.061$ $a/b = 0.74$		6.07 @ 700 nm $b/\lambda_0 = 0.057$ $a/b = 0.70$	5.37 @ 615 nm $b/\lambda_0 = 0.070$ $a/b = 0.69$
Copper (Cu)	7.41 @ 590 nm $b/\lambda_0 = 0.054$ $a/b = 0.82$	5.29 @ 590 nm $b/\lambda_0 = 0.070$ $a/b = 0.72$	8.42 @ 690 nm $b/\lambda_0 = 0.051$ $a/b = 0.80$	5.28 @ 695 nm $b/\lambda_0 = 0.062$ $a/b = 0.72$	4.51 @ 700 nm $b/\lambda_0 = 0.070$ $a/b = 0.80$	5.93 @ 700 nm $b/\lambda_0 = 0.058$ $a/b = 0.70$	8.42 @ 695 nm $b/\lambda_0 = 0.051$ $a/b = 0.80$

coats, gives diversity in optimal operational frequency. That is why CdS and TiO_2 coats exhibit considerable flexibility in their frequency preference in proportion to what is the metallic core inside. On the contrary, AlSb works always better with red color illumination regardless of the plasmonic medium that is paired. By inspection of Table I, it is also inferred that designs with the highest efficiency tend to be smaller since the incident power passing through their cross section is accordingly lower, which is the reason that very thin meta-atoms are excluded from the adopted scheme [36].

In Table II, we present nanoparticles with notable absorbing performances when the metallic material plays the role of the coat surrounding a dielectric sphere. Since the metal is sandwiched between two dielectrics (one of which is air), two surfaces between opposite-sign permittivities are formed and the field concentration around the external boundary ($r = b$) excites a similar surface plasmon around the internal one ($r = a$); therefore, the field in the lossy regions remains high, leading to substantial absorption. One can also notice that the majority of the presented meta-atoms in Table II are working better under red-colored illumination. Indeed, when the incident wave, traveling towards the nanosphere, meets the metallic layer, its penetration to the structure gets hindered by the mismatch of the oppositely signed $\mathrm{Re}[\varepsilon]$; therefore, maximal absorption occurs for large λ_0, overcoming such a skin effect (red color). Special mention can be made of the case of hollow plasmonic "nanobubbles" whose cores are empty (air inside) and which demonstrate high P_{abs}/P_{inc} due to the narrowly placed conformal surfaces, both separating metal from air. Finally, we note that silver's multicolor optimal response depending on what is the paired medium holds even if it plays the role of cladding (Table II) instead of core (Table I).

We notice that all the ultra-absorbing designs of Table I support a near-field distribution of the electric field magnitude $|\mathbf{E}|$ (normalized by the incident one), similar to the one shown in Fig. 2(a), when operated at the desired wavelength. In particular, we observe a large local field concentration along the x axis at the external boundary (between the dielectric and air), which sharpens the discontinuity of the normal (x) electric field component, happening due to material change. Furthermore, the field in the metallic core is not homogeneous (as in the static case) because of the substantial $|\mathrm{Im}[\varepsilon_1]|$ of the used metals at the optimal frequencies. Obviously, the contour plot is symmetric with respect to the z axis, unlike what is happening around the x axis, where the single-sided excitation biases the distributions. The arrows on the map show the direction of the electric field components $(-\hat{\mathbf{y}} \times (\hat{\mathbf{y}} \times \mathbf{E}))$ being parallel to the (z, x) plane and it is interesting that the in-plane electric field changes direction into the metallic core. In Fig. 2(b), we consider the same particle and represent the typical variation of total $|\mathbf{H}|$ on the (z, x) plane (which, unlike $|\mathbf{E}|$, is continuous), while the vector field corresponds to $(-\hat{\mathbf{y}} \times (\hat{\mathbf{y}} \times \mathbf{H}))$. One directly observes the two hotspots along the z axis at the interface between the plasmonic core and the dielectric coat, which is a manifestation of a localized surface plasmon [8]. It is also remarkable that, under the maximal absorption condition, the z component of the magnetic field into the core is much stronger than the x one and even larger than the main y one.

When it comes to the highly absorbing nanospheres employing a metallic shell and a semiconducting core referred to in Table II, a representative electric field response is shown in Fig. 3(a). Again, the signal is maximized at $x = \pm b$ but, unlike in Fig. 2(a), the dielectric cavity sustains significant intensity due to its nonplasmonic ($\mathrm{Re}[\varepsilon_1] > 0$) nature. In addition, the electric field in the low-loss core is almost homogeneous and parallel to the incident component (x), which reminds us clearly of the static solution (unlike the highly damped

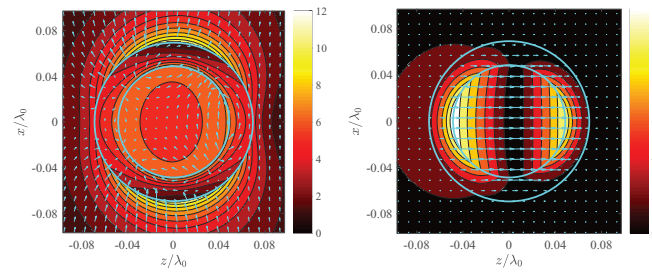

FIG. 2. Typical spatial distribution of the normalized magnitude of (a) total electric field $|\mathbf{E}|$ and (b) total magnetic field $|\mathbf{H}|$ on the (z, x) plane for most core-shell designs of Table I. The specific outputs belong to Cu/GaP nanospheres at $\lambda_0 = 640$ nm. The arrows show the direction of the in-plane components of the corresponding fields.

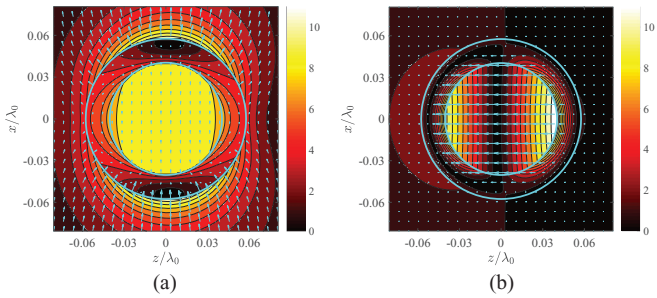

FIG. 3. Typical spatial distribution of the normalized magnitude of (a) total electric field $|\mathbf{E}|$ and (b) total magnetic field $|\mathbf{H}|$ on the (z, x) plane for most shell-core designs of Table II. The specific outputs belong to a GaP/Au nanosphere at $\lambda_0 = 700\,\text{nm}$. The arrows show the direction of the in-plane field components of the corresponding fields.

case of Fig. 2(a)). In Fig. 3(b), where $|\mathbf{H}(z, x)|$ is represented, we notice again [as in Fig. 2(b)] the localized plasmon at $z = \pm a$, but this time the signal magnitude at the rear side $(z = a)$ is stronger than the one at the front side $(z = -a)$, contrary to what is recorded for the nanosphere with plasmonic core. Importantly, the dielectric internal texture of the meta-atom flips the direction of the dominant magnetic (z) component compared to Fig. 2(b), while the density remains homogeneous.

In Fig. 4(a), we show the metric $P_{\text{abs}}/P_{\text{inc}}$ as a function of the working wavelength λ_0 for selected optimally absorbing designs of Table I. It is noteworthy that all four nanospheres, which are picked based on their large performance and operated at various frequencies, have a silver core (as indicated by the corresponding multicolored row of Table I). Furthermore, we verify the well-known conclusion that the higher is the maximum at a resonance (Ag/GaP design, green color), the more narrow-band it is; in this way, highly selective filtering or switching is feasible with use of the respective particles. On the other hand, responses of less efficient designs (Ag/AlSb nanosphere, red color) give lower quality factors and support relatively high absorption for a wider range of wavelengths. In Fig. 4(b), the frequency response of various nanospheres with dielectric core and metallic cladding from Table II is represented with different colors corresponding to the optimal visible-light frequency. The selected designs for green (Ag/CdS) and violet (Ag/TiO_2) illumination yield very sharp transfer functions; however, the responses become smoother for devices operated at larger wavelengths.

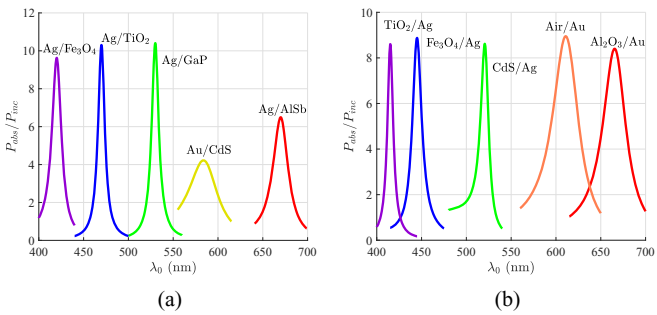

FIG. 4. Normalized absorbed power $P_{\text{abs}}/P_{\text{inc}}$ as a function of operational wavelength λ_0 for the best designs picked from (a) Table I, corresponding to nanospheres with metallic core and dielectric coat, and (b) Table II, corresponding to nanospheres with dielectric core and metallic coat.

IV. OPTIMAL SCATTERING

In Tables III and IV, we repeat the optimization process illustratively described in Figs. 1(b) and 1(c) for various combinations of materials, most of which are employed in Tables I and II, but in a quest for maximum scattering efficiency $P_{\text{scat}}/P_{\text{inc}}$ this time. Once again, we try metallic cores combined with semiconducting coatings, whose optimal designs are included in Table III (in direct analogy with Table I for absorption), and dielectric spheres covered by metals, whose results are shown in Table IV (similarly to Table II for absorption).

An important feature of Tables III and IV, which is absent in the case of absorption (Tables I and II), is that they are partially populated by homogeneous, instead of core-shell, particles. In particular, our optimization for specific material pairs shows that spheres solely filled by a single substance make more efficient designs rather than any alternative core-shell geometrical variant. For this reason, in Tables III and IV, we have repetitive occurrence of the same configurations comprising only one material. For example, one of the most highly scattering objects is a homogeneous GaP sphere when illuminated by blue light.

As usual, silver, due to its strong plasmonic features combined with low losses, gives very efficient core-shell nanospheres operated at various colors of the visible spectrum. It outperforms ($P_{\text{scat}}/P_{\text{inc}} \cong 11.2$) all its competitors working with violet light, when it is suitably covered by TiO_2 (Table III) and most remarkably scatters notably green ($P_{\text{scat}}/P_{\text{inc}} \cong 9.6$) and red ($P_{\text{scat}}/P_{\text{inc}} \cong 9.8$) illumination when used as an external coating to Al_2O_3 and CdS cores, respectively (Table IV). As far as the orange and yellow light is concerned, one can achieve significant scattering efficiencies by using copper spheres wrapped by Al_2O_3 layers (orange color, Table III) or copper claddings around CdTe cores (yellow color, Table IV).

In Fig. 5(a), we show the electric field magnitude variation $|\mathbf{E}|$ on the (z, x) plane as in Figs. 2(a) and 3(a) but for a representative case of maximally scattering homogeneous dielectric spheres. We notice again the two substantial signal concentrations along the x axis at the external boundary of the shell indicating discontinuity of the normal (x-directed) components. The internal distribution is almost symmetric azimuthally with a slight shift, as an outcome of the unilateral excitation, giving a dark point close to the origin. As far as the direction of the in-plane $\mathbf{E}$ is concerned [arrows in Fig. 5(a)], one can observe vortices [57] around that dark point which extend across the considered cross section of the sphere.

Most of the other optimal core-shell nanoparticles of Tables III and IV are scattering light like a vertical (along the x axis) electric dipole operated at its resonance as shown in Figs. 2(a) and 3(a), while their magnetic fields $\mathbf{H}$ form the well-known localized surface plasmon (along the z axis) depicted in Figs. 2(b) and 3(b). The same effects occur and are even more enhanced when the optimization concludes

TABLE III. Optimally scattering (maximum P_{scat}/P_{inc}) nanospheres with metallic cores (ε_1, different rows) and dielectric shells (ε_2, different columns).

SCATTERING Core/Shell	**Aluminium(III) oxide (Al_2O_3)**	**Aluminium antimonide (AlSb)**	**Cadmium sulfide (CdS)**	**Cadmium telluride (CdTe)**	**Gallium phosphide (GaP)**	**Titanium dioxide (TiO_2)**
Silver (Ag)	9.35 @ 400 nm $b/\lambda_0 = 0.098$ $a/b = 0.86$	8.54 @ 700 nm $b/\lambda_0 = 0.10$ $a/b = 0.74$	9.61 @ 540 nm $b/\lambda_0 = 0.010$ $a/b = 0.67$	7.80 @ 400 nm Ag only $b/\lambda_0 = 0.12$	11.45 @ 485 nm $b/\lambda_0 = 0.19$ $a/b = 0.20$	11.17 @ 425 nm $b/\lambda_0 = 0.086$ $a/b = 0.86$
Gold (Au)	4.85 @ 605 nm $b/\lambda_0 = 0.15$ $a/b = 0.80$	8.09 @ 700 nm AlSb only $b/\lambda_0 = 0.13$	6.80 @ 680 nm $b/\lambda_0 = 0.13$ $a/b = 0.65$		10.13 @ 475 nm GaP only $b/\lambda_0 = 0.13$	7.08 @ 400 nm TiO_2 only $b/\lambda_0 = 0.18$
Copper (Cu)	5.14 @ 605 nm $b/\lambda_0 = 0.146$ $a/b = 0.78$	8.09 @ 700 nm AlSb only $b/\lambda_0 = 0.13$	7.01 @ 645 nm $b/\lambda_0 = 0.126$ $a/b = 0.70$	4.91 @ 610 nm $b/\lambda_0 = 0.142$ $a/b = 0.92$	10.13 @ 475 nm GaP only $b/\lambda_0 = 0.13$	7.08 @ 400 nm TiO_2 only $b/\lambda_0 = 0.18$

to a single metallic sphere since they keep their internal electric field very low. On the contrary, the design examined in Fig. 5(b) (Ag/GaP at $\lambda_0 = 485$ nm) makes an exception in terms of its near-field pattern since its small core leaves the dielectric mantle to support two maxima along the z axis into its volume. In addition, the vector $(-\hat{\mathbf{y}} \times (\hat{\mathbf{y}} \times \mathbf{E}))$ follows again a dipolar pattern but the field lines depart from and arrive at points with small field intensity. As a result, there is a remarkable inversion of the background local electric field in the vicinity of the meta-atom, which can be attributed to the considerable electrical size of our sphere combined with its high scattering efficiency.

In Fig. 5(c), we have picked some efficient scatterers from Tables III and IV which require a single medium (dielectric) and examine the variation of their performance P_{scat}/P_{inc} as a function of oscillation wavelength λ_0 operated at several colors of the visible spectrum (indicated by the color of the respective curves as in Fig. 4). One clearly notices the well-known trade-off between the magnitude and the bandwidth of the resonance which gives a quite selective transfer function for the GaP nanosphere and a wideband response for a homogeneous CdS particle. Similarly, in Fig. 5(d), we consider various core-shell designs and we realize that the one with the near field of Fig. 5(b) (Ag/GaP) supports an extremely sharp resonance which renders it suitable for switching and filtering applications. When it comes to the rest of the setups, their operations are more narrow band compared to their homogeneous counterparts, while their maximum P_{scat} is kept close to tenfold the incident power P_{inc}.

V. OPTIMAL CLOAKING

In this section, we repeat the optimization process described in Sec. II B and executed in Sec. IV by aiming at the minimization of P_{scat}/P_{inc} instead of the maximization of it. In other words, we are searching for pairs of media which make core-shell nanospheres exhibit very low scattering efficiencies while having a non-negligible optical diameter $2b/\lambda_0$. As imposed by the principles of a scattering cancellation cloak [16], opposite signs of permittivities are required ($\mathrm{Re}[\varepsilon_1]\mathrm{Re}[\varepsilon_2] < 0$) in order for the entire particle to become transparent. However, in this study we do not follow exactly the scattering cancellation paradigm [16] due to the constraint for minimum size ($b > 0.05\lambda_0$) and inevitable losses. Indeed, in the lossless limit, the true minimum is $P_{scat} \to 0$ and occurs for an extremely tiny sphere $b/\lambda_0 \to 0$, which is rejected by

TABLE IV. Optimally scattering (maximum P_{scat}/P_{inc}) nanospheres with dielectric cores (ε_1, different columns) and metallic shells (ε_2, different rows).

SCATTERING Shell/Core	**Aluminium(III) oxide (Al_2O_3)**	**Aluminium antimonide (AlSb)**	**Cadmium sulfide (CdS)**	**Cadmium telluride (CdTe)**	**Gallium phosphide (GaP)**	**Titanium dioxide (TiO_2)**
Silver (Ag)	9.62 @ 530 nm $b/\lambda_0 = 0.082$ $a/b = 0.78$	8.09 @ 700 nm AlSb only $b/\lambda_0 = 0.13$	9.82 @ 700 nm $b/\lambda_0 = 0.083$ $a/b = 0.83$	7.80 @ 400 nm Ag only $b/\lambda_0 = 0.12$	10.13 @ 475 nm GaP only $b/\lambda_0 = 0.13$	9.71 @ 650 nm $b/\lambda_0 = 0.086$ $a/b = 0.80$
Gold (Au)	7.00 @ 700 nm $b/\lambda_0 = 0.11$ $a/b = 0.84$	8.09 @ 700 nm AlSb only $b/\lambda_0 = 0.13$		4.39 @ 565 nm Au only $b/\lambda_0 = 0.15$	10.13 @ 475 nm GaP only $b/\lambda_0 = 0.13$	7.08 @ 400 nm TiO_2 only $b/\lambda_0 = 0.18$
Copper (Cu)	6.92 @ 700 nm $b/\lambda_0 = 0.10$ $a/b = 0.84$	8.09 @ 700 nm AlSb only $b/\lambda_0 = 0.13$	6.38 @ 590 nm CdS only $b/\lambda_0 = 0.19$	4.47 @ 590 nm Cu only $b/\lambda_0 = 0.15$	10.13 @ 475 nm GaP only $b/\lambda_0 = 0.13$	7.08 @ 400 nm TiO_2 only $b/\lambda_0 = 0.18$

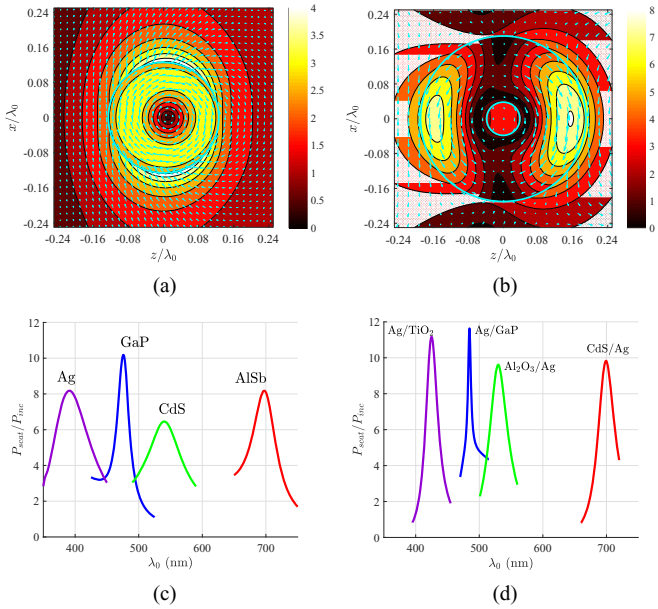

FIG. 5. (a, b) Spatial distribution of the normalized magnitude of the total electric field $|\mathbf{E}|$ for (a) typical homogeneous dielectric sphere maximal scattering design (AlSb alone at $\lambda_0 = 700$ nm) and (b) optimal particle with silver core and GaP shell (at $\lambda_0 = 485$ nm). The arrows show the direction of the in-plane electric field vector. (c, d) Normalized absorbed power $P_{\text{scat}}/P_{\text{inc}}$ as a function of operational wavelength λ_0 for certain designs picked from Tables III and IV.

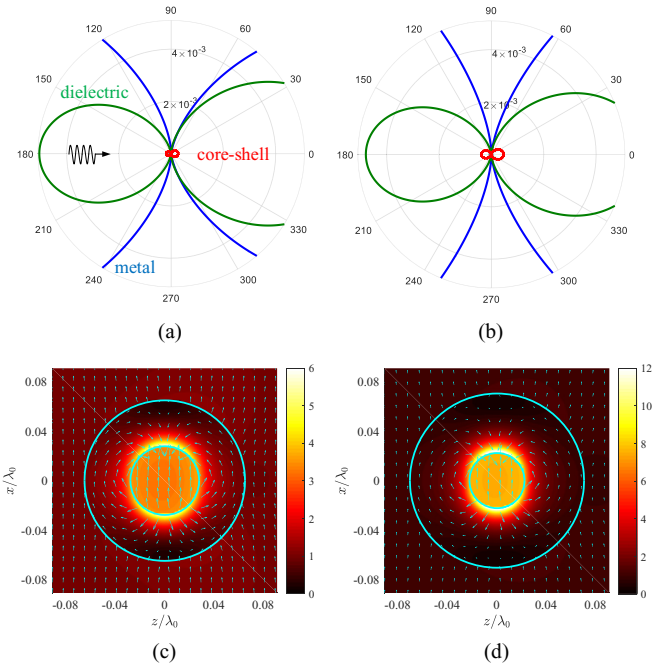

FIG. 6. (a, b) The radiation patterns $[r^2 p_{\text{scat}}(r,\theta,\varphi)/P_{\text{inc}}]$ for spherical nanoparticles of the same external radius: homogeneous metallic (blue), homogeneous dielectric (green), and cloaked core-shell (red). (c, d) The respective near-field spatial distributions of $|\mathbf{E}|$; the arrows represent the in-plane vector of electric field. Panels (a) and (c) correspond to the Ag/GaP pair (at $\lambda_0 = 645$ nm) and panels (b) and (d) to the Ag/TiO_2 combination (at $\lambda_0 = 525$ nm) of Table V.

our scheme. Our objective is not to cloak a specific volume of radius a and permittivity ε_1 but to propose nanospheres of external radius b that scatter a negligible portion of the incoming power corresponding to their geometrical cross section (πb^2). Finally, it is important to clarify that our method does not give efficient designs with dielectric core and metallic cladding due to the mismatch of the wave in vacuum with the plasmonic coat, which gives rise to a skin effect and prevents the incident wave from "seeing" the volume average of the structure.

In Table V, we show the least scattering nanoparticles with plasmonic core coated by semiconducting mantles for each combination of the considered media. Once again, we notice the substantial ability of silver spheres to provide optimal designs (scattering less than 0.5% of P_{inc}) at different colors of the visible spectrum depending on what is the dielectric cladding that contains them. Furthermore, the nanoparticles with gold and copper core working for red color are almost identical regardless of the coating (Fe_2O_3 or GaAs) since the two metals have similar permittivities at $\lambda_0 \cong 700$ nm: $\varepsilon_1 \cong -18 - i0.85$.

In Fig. 6(a), we pick a specific low-scattering design (Ag/GaP at $\lambda_0 = 645$ nm) from Table V of size ($2b$) and represent certain radiation patterns, namely, the power density $p_{\text{scat}}(r,\theta,\varphi)$ (which is obviously inversely proportional to r^2), multiplied by r^2 to neutralize the effect of the distance, and divided by the incident power P_{inc}. In other words, we

TABLE V. Optimally cloaked (minimum $P_{\text{scat}}/P_{\text{inc}}$) nanospheres with metallic cores (ε_1, different rows) and dielectric shells (ε_2, different columns). The scattering cancellation cloak [16] under realistic losses in the visible.

CLOAKING Core/Shell	Aluminium(III) oxide (Al_2O_3)	Cadmium sulfide (CdS)	Iron(III) Oxide (Fe_2O_3)	Iron(II,III) Oxide (Fe_3O_4)	Gallium arsenide (GaAs)	Gallium phosphide (GaP)	Titanium dioxide (TiO_2)
Silver (Ag)	0.018 @ 425 nm $b/\lambda_0 = 0.12$ $a/b = 0.32$	0.004 @ 535 nm $b/\lambda_0 = 0.075$ $a/b = 0.35$	0.023 @ 635 nm $b/\lambda_0 = 0.076$ $a/b = 0.39$	0.054 @ 515 nm $b/\lambda_0 = 0.11$ $a/b = 0.39$	0.024 @ 700 nm $b/\lambda_0 = 0.074$ $a/b = 0.52$	0.002 @ 645 nm $b/\lambda_0 = 0.064$ $a/b = 0.43$	0.003 @ 525 nm $b/\lambda_0 = 0.070$ $a/b = 0.32$
Gold (Au)		0.034 @ 600 nm $b/\lambda_0 = 0.11$ $a/b = 0.44$	0.024 @ 685 nm $b/\lambda_0 = 0.077$ $a/b = 0.39$		0.034 @ 695 nm $b/\lambda_0 = 0.090$ $a/b = 0.64$		0.031 @ 595 nm $b/\lambda_0 = 0.10$ $a/b = 0.44$
Copper (Cu)		0.018 @ 605 nm $b/\lambda_0 = 0.094$ $a/b = 0.42$	0.021 @ 685 nm $b/\lambda_0 = 0.079$ $a/b = 0.40$		0.033 @ 700 nm $b/\lambda_0 = 0.090$ $a/b = 0.64$		0.019 @ 605 nm $b/\lambda_0 = 0.094$ $a/b = 0.42$

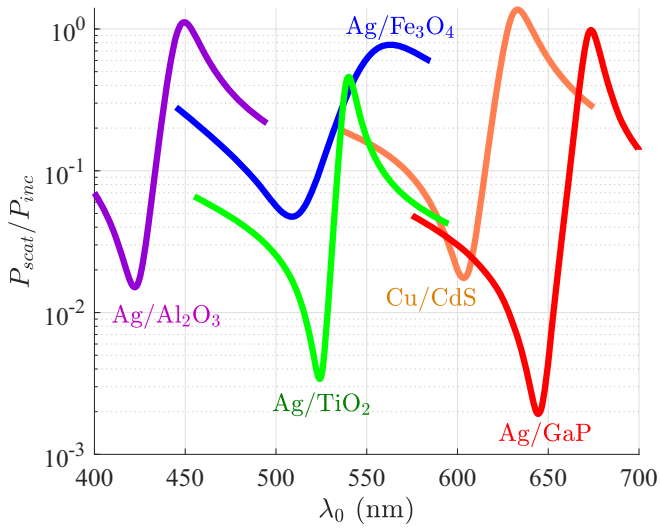

FIG. 7. The variation of $P_{\text{scat}}/P_{\text{inc}}$ with respect to operational wavelength λ_0 for several optimally cloaked nanoparticles picked from Table V working at different colors of the visible spectrum. Asymmetric (Fano) resonances [7] occur.

have $\int_0^{2\pi}\int_0^{\pi}[r^2 p_{\text{scat}}/P_{\text{inc}}]\sin\theta d\theta d\phi = P_{\text{scat}}/P_{\text{inc}}$ and show the variation of the quantity in the brackets at the maximum cross section plane. We consider three objects of the same external radius b and accordingly the same normalization power P_{inc}: two homogeneous spheres filled either with the used plasmonic material (Ag, ε_1) or with the employed dielectric (GaP, ε_2) and the core-shell design which optimally combines these two (ε_1, ε_2) media to make a practically cloaked object with identical dimensions. The latter polar plot is negligible in magnitude compared to the two former ones and that is why we show only parts from the radiation patterns of the two homogeneous spheres. In Fig. 6(b), the same process of Fig. 6(a) is repeated but for the particle with silver core and TiO_2 cladding. As indicated in Table V, the core-shell scattering is slightly larger that time, but simultaneously vastly smaller than the $P_{\text{scat}}/P_{\text{inc}}$ from silver or TiO_2 homogeneous spheres of radius $b \cong 37$ nm at $\lambda_0 = 525$ nm.

In Figs. 6(c) and 6(d), we show the near-field distributions $|\mathbf{E}|$ for the cloaked objects examined in Figs. 6(a) and 6(b), respectively. In both designs we note the almost homogeneous electric field outside of them which is also x directed as indicated by the in-plane arrows. In other words, the incident plane wave is practically unperturbed not only in the far region [as shown in Figs. 6(a) and 6(b)] but also in the vicinity of the external surface $r = b$, implying an almost perfect scattering cancellation cloak with realistic losses. In addition, the signal is homogeneous into the core, as dictated by the spherical symmetry, and quite strong, as a result of electric dipole resonances that develop almost opposite ($\text{Re}[\varepsilon_1]\text{Re}[\varepsilon_2] < 0$) and mutually neutralized polarizations at the two domains of the particle.

In Fig. 7, as in the other sections, we select some of the best designs of the related Table V and test them in the vicinity of their optimal operational frequency. Some of the optimal particles (like Ag/GaP under red light) retain their notable performance at much smaller λ_0 giving wideband cloaks. However, it is remarkable that, in all cases, the minimal-scattering bands are followed by "bright zones" at slightly larger wavelengths resulting in an asymmetric line shape that unveils the Fano-resonant nature [7] of the cloaking effects reported in Table V. In this way, one obtains a dramatic two-decimal-order upsurge of P_{scat} (Ag/TiO_2 design under green light) if increases the oscillating wavelength only by a few nanometers.

VI. CONCLUSIONS

An exhaustive search for core-shell spherical particles that exhibit substantial efficiency in terms of absorption and scattering of the incoming light has been presented. Numerous plasmonics, semiconductors, and dielectrics have been considered as potential homogeneous fillings of the two domains comprising the nanospheres. For each pair of media, we scan the entire visible wavelength spectrum and select the sizes that give maximal performance to the regarded simple architecture. These optimal designs are reported in several tables, in proportion to the objective they serve, while their near-field representations reveal the underlying wave interactions. By inverse logic, we quest after poor (minimal) scattering efficiency corresponding to invisible objects; as a result, many realistic scattering-cancellation cloaks under actual losses have been obtained.

The major mechanisms behind almost any performance maximization of both isolated particles and collective metasurfaces are the various types of resonances. Since the employed materials are lossy and the behavior of the meta-atoms is strongly dependent on the optical sizes, no closed-form conditions for resonance can be derived and, thus, the proposed technique is required to detect the occurrence of similar effects by optimizing the considered metrics. Therefore, in the cases of most ultraperforming designs, we observe electric or magnetic Mie resonances corresponding to maximal dipolar terms in the sums of the canonical solutions. Needless to say, quadruple or higher-order resonances emerge as long as the electrical radius of the particles increases, and multiple non-negligible canonical terms support strong local maxima. Furthermore, our method frequently stumbles on optimal nanospheres with field hotspots attributed to localized surface plasmon resonances developed at boundaries of opposite-sign permittivity domains. Such plasmonic effective behavior is also a prerequisite for the particle to be seen as transparent, namely, to demonstrate invisibility with vanishing scattered power. These minima in the output can appear at wavelengths neighboring to corresponding maxima, yielding to frequency responses with asymmetric shape indicating Fano resonances.

This work detects the limits of a simple particle configuration into a parametric space, permitting it to be employed in virtually all metasurface applications in the visible. The presented designs provide performance benchmarks of what one can achieve with core-shell geometry and, simultaneously, set the bars that one must pass by utilizing more complex structures and artificial media. However, even a plain increase in the number of concentric shells will render the full, "brute-force" optimization of the system computationally challenging, and thus should be assisted by more elaborate techniques like the implementation of machine learning algorithms.

ACKNOWLEDGMENT

This work was partially supported by Nazarbayev University Small Grants with the project entitled "Super transmitters, radiators and lenses via photonic synthetic matter" (Project No. 090118FD5349). Funding from the MES RK state-targeted program BR05236454 is also acknowledged.

[1] C. L. Holloway, E. F. Kuester, J. A. Gordon, J. O'Hara, J. Booth, and D. R. Smith, An overview of the theory and applications of metasurfaces: The two-dimensional equivalents of metamaterials, IEEE Antennas Propag. Mag. **54**, 10 (2012).

[2] N. Yu and F. Capasso, Flat optics with designer metasurfaces, Nat. Mater. **13**, 139 (2014)

[3] N. Engheta, Circuits with light at nanoscales: Optical nanocircuits inspired by metamaterials, Science **317**, 1698 (2007).

[4] A. Arbabi, Y. Horie, M. Bagheri, and A. Faraon, Dielectric metasurfaces for complete control of phase and polarization with subwavelength spatial resolution and high transmission, Nat. Nanotechnol. **10**, 937 (2015).

[5] J. Zhou, A. Panday, Y. Xu, X. Chen, L. Chen, C. Ji, and L. J. Guo, Visualizing Mie Resonances in Low-Index Dielectric Nanoparticles, Phys. Rev. Lett. **120**, 253902 (2018).

[6] A. B. Evlyukhin, S. M. Novikov, U. Zywietz, R. L. Eriksen, C. Reinhardt, S. I. Bozhevolnyi, and B. N. Chichkov, Demonstration of magnetic dipole resonances of dielectric nanospheres in the visible region, Nano Lett. **12**, 3749 (2012).

[7] A. E. Miroshnichenko, S. Flach, and Y. S. Kivshar, Fano resonances in nanoscale structures, Rev. Mod. Phys. **82**, 2257 (2010).

[8] V. Amendola, R. Pilot, M. Frasconi, O. M. Marago, and M. A. Iati, Surface plasmon resonance in gold nanoparticles: A review, J. Phys.: Condens. Matter **29**, 203002 (2017).

[9] D. C. Tzarouchis and A. Sihvola, General scattering characteristics of resonant core-shell spheres, IEEE Trans. Antennas Propag. **66**, 323 (2018).

[10] R. E. Hamam, A. Karalis, J. D. Joannopoulos, and M. Soljačić, Coupled-mode theory for general free-space resonant scattering of waves, Phys. Rev. A **75**, 053801 (2007).

[11] Z. Ruan and S. Fan, Design of subwavelength superscattering nanospheres, Appl. Phys. Lett. **98**, 043101 (2011).

[12] A. E. Miroshnichenko and M. I. Tribelsky, Ultimate Absorption in Light Scattering by a Finite Obstacle, Phys. Rev. Lett. **120**, 033902 (2018).

[13] Y. Huang and L. Gao, Superscattering of light from core-shell nonlocal plasmonic nanoparticles, J. Phys. Chem. C **118**, 30170 (2014)

[14] T. J. Antosiewicz, S. P. Apell, and T. Shegai, Plasmon-exciton interactions in a core-shell geometry, ACS Photon. **1**, 454 (2014)

[15] V. G. Kravets, S. Neubeck, A. N. Grigorenko, and A. F. Kravets, Plasmonic blackbody: Strong absorption of light by metal nanoparticles embedded in a dielectric matrix, Phys. Rev. B **81**, 165401 (2010).

[16] A. Alù and N. Engheta, Achieving transparency with plasmonic and metamaterial coatings, Phys. Rev. E **72**, 016623 (2005).

[17] F. Monticone and A. Alù, Do Cloaked Objects Really Scatter Less?, Phys. Rev. X **3**, 041005 (2013).

[18] P. Yu, Y. Yao, J. Wu, X. Niu, A. L. Rogach, and Z. Wang, Effects of plasmonic metal core-dielectric shell nanoparticles on the broadband light absorption enhancement in thin film solar cells, Sci. Rep. **7**, 7696 (2017).

[19] X.-C. Ma, Y. Dai, L. Yu, and B.-B. Huang, Energy transfer in plasmonic photocatalytic composites, Light Sci. Appl. **5**, e16017 (2016).

[20] B. Khlebtsov, V. Zharov, A. Melnikov, V. Tuchin, and N. Khlebtsov, Optical amplification of photothermal therapy with gold nanoparticles and nanoclusters, Nanotechnology **17**, 5167 (2006).

[21] Q. Meng, J. Meng, W. Ran, J. Wang, Y. Zhai, P. Zhang, and Y. Li, Light-activated core-shell nanoparticles for spatiotemporally specific treatment of metastatic triple-negative breast cancer, ACS Nano **12**, 2789 (2018).

[22] F. Wang, R. Deng, J. Wang, Q. Wang, Y. Han, H. Zhu, X. Chen, and X. Liu, Tuning upconversion through energy migration in core-shell nanoparticles, Nat. Mater. **10**, 968 (2011).

[23] F. Monticone, C. Argyropoulos, and A. Alù, Multilayered Plasmonic Covers for Comblike Scattering Response and Optical Tagging, Phys. Rev. Lett. **110**, 113901 (2013).

[24] C. Argyropoulos, P.-Y. Chen, F. Monticone, G. D'Aguanno, and A. Alù, Nonlinear Plasmonic Cloaks to Realize Giant All-Optical Scattering Switching, Phys. Rev. Lett. **108**, 263905 (2012).

[25] Y. Pu, R. Grange, C.-L. Hsieh, and D. Psaltis, Nonlinear Optical Properties of Core-Shell Nanocavities for Enhanced Second-Harmonic Generation, Phys. Rev. Lett. **104**, 207402 (2010).

[26] T. B. Hoang, G. M. Akselrod, C. Argyropoulos, J. Huang, D. R. Smith, and M. H. Mikkelsen, Ultrafast spontaneous emission source using plasmonic nanoantennas, Nat. Commun. **6**, 7788 (2015).

[27] H.-W. Ko, M.-H. Chi, C.-W. Chang, C.-W. Chu, K.-H. Luo, and J.-T. Chen, Fabrication of core-shell polymer nanospheres in the nanopores of anodic aluminum oxide templates using polymer blend solutions, ACS Macro Lett. **4**, 717 (2015).

[28] R. T. Tom, A. S. Nair, N. Singh, M. Aslam, C. L. Nagendra, R. Philip, K. Vijayamohanan, and T. Pradeep, Freely dispersible Au@TiO_2, Au@ZrO_2, Ag@TiO_2, and Ag@ZrO_2 core-shell nanoparticles: One-step synthesis, characterization, spectroscopy, and optical limiting properties, Langmuir **19**, 3439 (2003).

[29] R. Fleury, J. Soric, and A. Alù, Physical bounds on absorption and scattering for cloaked sensors, Phys. Rev. B **89**, 045122 (2014).

[30] O. D. Miller, C. W. Hsu, M. T. H. Reid, W. Qiu, B. G. DeLacy, J. D. Joannopoulos, M. Soljačić, and S. G. Johnson, Fundamental Limits to Extinction by Metallic Nanoparticles, Phys. Rev. Lett. **112**, 123903 (2014).

[31] J. Peurifoy, Y. Shen, L. Jing, Y. Yang, F. Cano-Renteria, B. G. DeLacy, J. D. Joannopoulos, M. Tegmark, and M. Soljačić, Nanophotonic particle simulation and inverse design using artificial neural networks, Sci. Adv. **4**, eaar4206 (2018).

[32] S. Molesky, Z. Lin, A. Y. Piggott, W. Jin, J. Vuckovic, and A. W. Rodriguez, Outlook for inverse design in nanophotonics, Nat. Photon. **12**, 659 (2018).

[33] C. F. Bohren and D. R. Huffman, *Absorption and Scattering of Light by Small Particles* (Wiley, New York, 1983).

[34] L. Ranno, S. Dal Forno, and J. Lischner, Computational design of bimetallic core-shell nanoparticles for hot-carrier photocatalysis, NPJ Comput. Mater. **4**, 31 (2018).

[35] A. Andryieuski, A. V. Lavrinenko, M. Petrov, and S. A. Tretyakov, Homogenization of metasurfaces formed by random resonant particles in periodical lattices, Phys. Rev. B **93**, 205127 (2016).

[36] Z. Ruan and S. Fan, Superscattering of Light from Subwavelength Nanostructures, Phys. Rev. Lett. **105**, 013901 (2010).

[37] http://refractiveindex.info/

[38] D. E. Aspnes and A. A. Studna, Dielectric functions and optical parameters of Si, Ge, GaP, GaAs, GaSb, InP, InAs, and InSb from 1.5 to 6.0 eV, Phys. Rev. B **27**, 985 (1983).

[39] A. D. Rakić, A. B. Djurišić, J. M. Elazar, and M. L. Majewski, Optical properties of metallic films for vertical-cavity optoelectronic devices, Appl. Opt. **37**, 5271 (1998).

[40] H. Hovel, S. Fritz, A. Hilger, V. Kreibig, and M. Vollmer, Width of cluster plasmon resonances: Bulk dielectric functions and chemical interface damping, Phys. Rev. B **48**, 18178 (1993).

[41] A. Abrashuly and C. Valagiannopoulos, Limits for Absorption and Scattering by Core-Shell Nanowires in the Visible Spectrum, Phys. Rev. Appl. **11**, 014051 (2019).

[42] I. Liberal and N. Engheta, Near-zero refractive index photonics, Nat. Photon. **11**, 149 (2017).

[43] I. I. Smolyaninov and V. N. Smolyaninova, Metamaterial superconductors, Phys. Rev. B **91**, 094501 (2015).

[44] Y. Ra'di, V. S. Asadchy, and S. A. Tretyakov, One-way transparent sheets, Phys. Rev. B **89**, 075109 (2014).

[45] P. Mélinon, S. Begin-Colin, J. L. Duvail, F. Gauffre, N. H. Boime, G. Ledoux, J. Plain, P. Reiss, F. Silly, and B. Warot-Fonrose, Engineered inorganic core/shell nanoparticles, Phys. Rep. **543**, 163 (2014).

[46] Y. Zhou and H. Wang, An $Al@Al_2O_3@SiO_2$/polyimide composite with multilayer coating structure fillers based on self-passivated aluminum cores, Appl. Phys. Lett. **102**, 132901 (2013).

[47] L. M. Liz-Marzán, M. Giersig, and P. Mulvaney, Synthesis of nanosized gold-silica core-shell particles, Langmuir **12**, 4329 (1996).

[48] L. Xu, M. Sun, W. Ma, H. Kuang, and C. Xu, Self-assembled nanoparticle dimers with contemporarily relevant properties and emerging applications, Mater. Today **19**, 595 (2016).

[49] L. Malassis, P. Massé, M. Tréguer-Delapierre, S. Mornet, P. Weisbecker, V. Kravets, A. Grigorenko, and P. Barois, Bottom-up fabrication and optical characterization of dense films of meta-atoms made of core-shell plasmonic nanoparticles, Langmuir **29**, 1551 (2013).

[50] D. Kosters, A. de Hoogh, H. Zeijlemaker, H. Acar, N. Rotenberg, and L. Kuipers, Core-shell plasmonic nanohelices, ACS Photon. **4**, 1858 (2017).

[51] A. Rahimzadegan, C. Rockstuhl, and I. Fernandez-Corbaton, Core-Shell Particles as Building Blocks for Systems with High Duality Symmetry, Phys. Rev. Appl. **9**, 054051 (2018).

[52] O. Waser, R. Büchel, A. Hintennach, P. Novák, and S. E. Pratsinis, Continuous flame aerosol synthesis of carbon-coated nano-$LiFePO_4$ for Li-ion batteries, J. Aerosol Sci. **42**, 657 (2011).

[53] F. Bao, J.-L. Yao, and R.-A. Gu, Synthesis of magnetic Fe_2O_3/Au core/shell nanoparticles for bioseparation and immunoassay based on surface-enhanced Raman spectroscopy, Langmuir **25**, 10782 (2009).

[54] Y. Zhai, J. Zhai, Y. Wang, S. Guo, W. Ren, and S. Dong, Fabrication of iron oxide core/gold shell submicrometer spheres with nanoscale surface roughness for efficient surface-enhanced Raman scattering, J. Phys. Chem. C **113**, 7009 (2009).

[55] A. H. Hamad, L. Li, Z. Liu, X. L. Zhong, and T. Wang, Sequential laser and ultrasonic wave generation of $TiO_2@Ag$ core-shell nanoparticles and their anti-bacterial properties, Lasers Med. Sci. **31**, 263 (2016).

[56] P. R. West, S. Ishii, G. V. Naik, N. K. Emani, V. M. Shalaev, and A. Boltasseva, Searching for better plasmonic materials, Laser Photon. Rev. **4**, 795 (2010).

[57] R. Paniagua-Domínguez, F. Lopez-Tejeira, R. Marques, and J. A. Sanchez-Gil, Metallo-dielectric core-shell nanospheres as building blocks for optical three-dimensional isotropic negative-index metamaterials, New J. Phys. **13**, 123017 (2011).